PHOTONICS Research

Broadly tunable lens-coupled nonlinear quantum cascade lasers in the sub-THz to THz frequency range

Kazuue Fujita,* Shohei Hayashi, Akio Ito, Tatsuo Dougakiuchi, Masahiro Hitaka, and Atsushi Nakanishi

Central Research Laboratory, Hamamatsu Photonics K.K., 5000 Hirakuchi, Hamakita Ward, Hamamatsu 434-8601, Japan
**Corresponding author: kfujita@crl.hpk.co.jp*

Received 20 September 2021; revised 18 December 2021; accepted 10 January 2022; posted 11 January 2022 (Doc. ID 443819); published 22 February 2022

Room-temperature terahertz (THz) quantum cascade laser sources with intracavity difference-frequency nonlinear mixing are electrically pumped monolithic semiconductor laser sources operating in the 0.6–6 THz spectral range. We report widely tunable, low-frequency THz quantum cascade laser sources using a lens-coupled Cherenkov waveguide scheme. Based on a watt-class high-power, $\lambda \sim 13.7$ μm quantum cascade laser, the monolithic THz source is strongly coupled with a high-resistivity silicon lens, which causes a major increase in the THz coupling efficiency and demonstrates significant performance improvements. A room-temperature 1.5 THz device produces a 0.2 mW peak output power with a high-quality beam pattern. Improved THz outcoupling efficiency using the lens-coupled scheme enabled the demonstration of a high-performance external-cavity semiconductor THz source that is tunable from 420 GHz to 2 THz. The external-cavity, lens-coupled device configuration can technically be assembled into a butterfly-style package for a thumb-sized, widely frequency tunable THz semiconductor source.

https://doi.org/10.1364/PRJ.443819

1. INTRODUCTION

Room-temperature, broadly tunable, electrically pumped semiconductor sources for operation in the terahertz (THz) spectral range, which offer a similar operational simplicity to diode lasers, are highly desirable for a range of potential applications, including communications, imaging, spectroscopy, and chemical analysis [1,2]. With the drive toward widespread commercial use of THz technology, there is growing demand for a compact, tunable mass-producible coherent semiconductor source. On the low-frequency side of the THz range, many electron devices, including resonant tunnel diode (RTD) oscillators [3,4], heterojunction bipolar transistors (HBTs) [5,6], and CMOS transistors [7–9] have been developed to act as THz emitters. Simultaneously, on the high frequency side, a variety of technologies have been reported to date [10–13]. A THz quantum cascade laser (THz-QCL) is a powerful semiconductor source. The operating temperature of conventional THz-QCLs is improved at frequencies above 2 THz [14,15]. However, the laser's performance is highly limited in the lower frequency range; i.e., below 2 THz [16]. Recently, among efforts to develop room-temperature compact continuous wave (CW) sources, QCL-pumped molecular lasers have been proposed and demonstrated [17–19].

In addition, with regard to the frequency tunability of THz semiconductor sources, very wide frequency tuning over several hundred GHz is difficult to achieve for both electron devices and THz-QCLs. As compact semiconductor sources, uni-traveling-carrier photodiodes have demonstrated wide frequency tuning properties, mainly in the frequency range below 1 THz, with an average power of more than 1 μW [20]. These devices are used extensively in THz communications research [21]. Recently, QCL-pumped molecular lasers, which have potential for use as compact CW sources, have been shown to achieve wide frequency tuning over the range from 0.25 up to ~1 THz [18]. However, it is currently still challenging to realize a high-power, widely tunable THz semiconductor source for operation around 1.0 THz (i.e., at the center of the THz gap), in real-world applications.

THz-QCL sources with intracavity nonlinear difference frequency generation (DFG) mixing [22] are electrically pumped monolithic semiconductor sources operable at room temperature [23–27]. These room-temperature QCL devices have made dramatic advances in performance in recent years with use of active regions with properties that include giant second-order nonlinear susceptibility and the Cherenkov phase-matching scheme [28–30]. To date, these nonlinear QCL devices have allowed production of milliwatt-level output powers [26,27], wide frequency tunability [29,31–33], broadband terahertz emission [34], and comb generation [27,35,36]. Extremely wide frequency tuning between 1.2 THz and 5.9 THz has been demonstrated using an external cavity (EC) setup at room temperature [29,31]. Furthermore, THz imaging has also been demonstrated with these nonlinear QCL devices [37]. Because of their ultra-broadband emission spectra, the devices have also proven highly suitable for use in THz spectroscopic applications [38]. However, the performance of nonlinear QCLs tends to deteriorate in the low-frequency range below 2 THz [31]. Nevertheless, based on a long-wavelength dual-upper-state (DAU) active region design, we have demonstrated sub-THz nonlinear QCLs that produced output power of 11 μW at ~700 GHz at room temperature [39]. In addition, single-frequency operation of a 1.0 THz-QCL device also has been demonstrated at room temperature [40]. For operation at lower frequencies using QCL technology, intracavity millimeter wave emission has been observed with THz-QCLs at a temperature of 10 K [41].

Here, we report widely tunable, low-frequency THz nonlinear QCLs using a lens-coupled Cherenkov waveguide scheme, in which the device's semi-insulating InP substrate is closely appressed to a high-resistivity silicon (Si) lens. Because this leads to a major increase in the THz coupling efficiency, these sources demonstrate significant performance improvements. A 1.5 THz lens-coupled device based on a watt-class high-power, 13.7 μm mid-IR (MIR) QCL produced 0.2 mW peak output power at 288 K, along with a far-field beam pattern with an FWHM value of ~9° on both the fast and slow axes, while the same device without the Si-lens produced 60 μW peak power using two off-axis parabolic mirrors. The high terahertz generation efficiency and relaxed outcoupling conditions provided by the lens-coupled Cherenkov scheme allowed us to demonstrate a high-performance, EC THz-QCL source that was tunable between 0.42 and 2 THz.

2. DEVICE FABRICATION

In the experiment, the nonlinear QCL device is based on the DAU active region [30,42], which has a broadband gain bandwidth and very high nonlinearity for the low-frequency range. The lattice-matched $In_{0.53}Ga_{0.47}As/In_{0.52}Al_{0.48}As$ layer sequence for a single period of the active layers, starting from the injection barrier (i.e., toward the right), is given in angstroms as **34**/43/**20**/93/**9**/76/**10**/62/**11**/54/**12**/51/**13**/46/**15**/45/**17**/45/**22**/45/**27**/44, where the InAlAs barrier layers are in bold font, the InGaAs QW layers are in normal font, and the doped layers (Si, 1.5×10^{17} cm^{-3}) are underlined; further details about this nonlinear active region design are given in Ref. [39], while the active region doping is slightly reduced. This structure consists of 70 stages of lattice-matched QCL active region structures (total thickness: ~5.6 μm), and a semi-insulating InP wafer was used as the substrate for QCL growth. Growth of all the QCL structures was performed using the metal organic vapor phase epitaxy (MOVPE) technique. The growth process begins with the formation of a 200 nm thick InGaAs current spreading layer (Si, 1.0×10^{18} cm^{-3}) and a 5.0 μm thick n-InP (Si, 1.5×10^{16} cm^{-3}) film that is used as a lower cladding layer. The QCL active region is sandwiched between a 0.2 μm thick n-$In_{0.53}Ga_{0.47}As$ layer (Si, 1.5×10^{16} cm^{-3}) and a 0.45 μm thick n-$In_{0.53}Ga_{0.47}As$ layer (Si, 1.5×10^{16} cm^{-3}). The upper cladding layer consists of a 5 μm thick n-InP (Si, 1.5×10^{16} cm^{-3}) layer followed by a 15 nm thick n^{+}-InP (Si, $\sim 10^{18}$ cm^{-3}) cap layer. The wafer was processed into buried heterostructure waveguides with double-sided current extraction schemes. The buried heterostructure waveguide is critically important to improve the QCL performance. After laser ridge waveguide formation via dry and wet etching to a depth of ~15 μm, regrowth of the semi-insulating Fe:InP layer is performed by MOVPE to form a buried heterostructure. In our previous works, a Fe-doped InP buried layer was undergrown, with half of the depth (>3 μm) left unfilled to avoid overgrowth, as shown in Fig. 1(a). Because very thick active regions (>5 μm) are required to obtain the high output powers required for the long-wavelength QCL, it is still difficult to planarize the active region containing the Fe-doped InP buried layer. In this work, by optimizing the wet etching process used for ridge structure formation, we fabricate a thick Fe-doped InP layer for the buried heterostructure in which the active region is almost filled, as shown in Fig. 1(b). This approach reduces the waveguide losses of the long-wavelength QCL and also improves its thermal conductivity. The laser waveguide was designed to be a dielectric confinement structure for MIR light. The THz DFG emission is radiated into the semi-insulating InP substrate because of Cherenkov phase matching. A uniform single-period

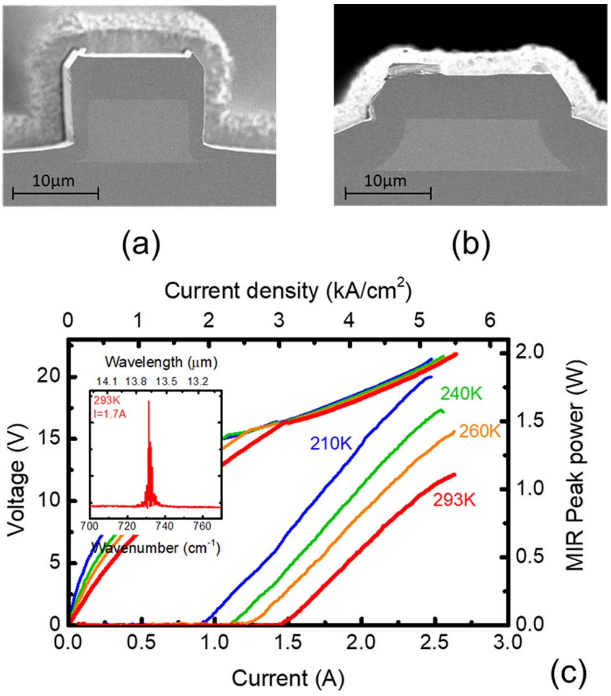

Fig. 1. Scanning electron microscope images of (a) a partially buried heterostructure quantum cascade laser (QCL) device and (b) the improved buried heterostructure device in this work. (c) Temperature-dependent mid-IR (MIR) light-current-voltage curves of a 13.7 μm quantum cascade laser. A room temperature emission spectrum is shown in the inset.

buried grating was defined for single-wavelength emission to achieve a distributed feedback (DFB)/Fabry–Pérot (FP) pump device configuration [34]. The grating period was designed to $\Lambda \sim 2.02$ μm via nanoimprint lithography and was etched to a depth of ~200 nm into the upper n-$In_{0.53}Ga_{0.47}As$ waveguide layers to provide feedback single-mode lasing at the MIR wavelength of $\lambda_{DFB} \sim 13$ μm, away from the FP lasing center at $\lambda_{FP} \sim 13.7$ μm; a similar procedure was described in our previous work [39].

Figure 1(c) shows the current-light-voltage ($I - L - V$) characterization of a 16 μm wide, 3 mm long, uncoated FP QCL device on a semi-insulating InP substrate operating in pulsed mode (pulse width = 250 ns; duty cycle = 2.5%) at various temperatures. The inset shows the lasing spectrum at 1.7 A. The FP (without the grating) device outputs a maximum power of 1.1 W (from a single facet) and a threshold current density of 3.0 kA/cm^2 at 293 K. The slope efficiency is 1.1 W/A at 293 K. The device performance is improved when compared to that of the previous device, which exhibited an output power of 0.76 W with a slope efficiency of 0.86 W/A. Although a high output power (830 mW) from a $\lambda = 14$ μm QCL with a diagonal transition and nonresonant extraction design has been reported previously [43], this is the highest peak power reported to date for long wavelength ($\lambda > 13$ μm) QCLs. High peak output power for a long-wavelength QCL with large transition dipole moments is essential for THz generation in the lower frequency range [39]. Note that the efficiency of the device on the semi-insulating substrate is reduced with an additional voltage drop because of side current injections that occur through the bottom contact. Besides, the side current injection scheme increases the thermal resistance of the devices. In fact, the maximum duty cycle of the devices is limited to approximately 10% at room temperature, which is similar to our previous devices [34], despite fabricating the full buried heterostructure. To achieve a higher duty cycle, epi-down mounting is necessary, as demonstrated for continuous wave nonlinear QCLs operating at higher frequencies [33]. However, it is not easy to apply devices with the side current injection scheme.

3. PERFORMANCE OF Si LENS-COUPLED DEVICE

In this work, a Si lens ($n_{Si} = 3.42$), which is nearly index-matched to both the QCL active region ($n_g = 3.46$) and the semi-insulating InP substrate ($n_{InP} \approx 3.52$), is placed in direct contact with the polished QCL device substrate to increase the THz outcoupling efficiency. Enhancement of the THz output powers due to increased radiation in the forward direction using the Si lens has been achieved in both QCL devices [44] and slot antennas on dielectric substrates [45], which radiate THz waves into the substrate and the air in accordance with the ratio of their dielectric constants, as reported previously. Further enhancement is obtained by increasing the beam directivity using the lens; as a result, this approach leads to higher output powers and improved beam patterns. In the THz-QCL source based on DFG, performance improvements with the use of high-resistivity Si materials have been demonstrated for transfer-printed devices on Si wafers [46]. This approach results in dramatic enhancement of both the THz outcoupling efficiency and the output power. However, as in this case, when n_g is higher than n_{Si}, it is difficult to adopt this approach since a Cherenkov phase-matching condition is not satisfied.

For ease of extraction of the THz radiation, the output front facet of the substrate of THz nonlinear QCL device was polished to an angle of 10°. Substrate polishing is required for two major reasons. First, it is necessary to avoid damaging the laser facet used for MIR lasing, and second, the major components of the generated THz power are distributed around the area within a distance of 100 μm from the active region. The output facet of the QCL device is projected from the carrier edge by 0.5 mm. The hyper-spherical Si lens has a diameter of 6 mm and a center thickness of 3.7 mm, with a high resistivity of $>1\ k\Omega \cdot cm$. The lens is designed to have a focal point at the near surface of the Si lens to collimate THz waves emitted from the device. This lens was pressed onto the polished facet of the device [Fig. 2(a)]. Direct contact between the lens and the device facet was critically important for THz power output extraction. The lens was positioned and pressed against the device

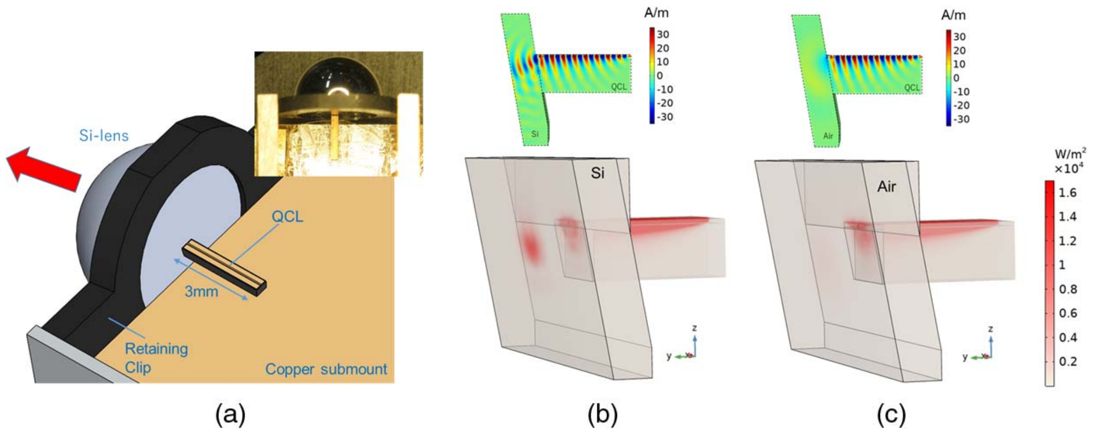

Fig. 2. (a) THz nonlinear QCL device with abutted Si lens. (b), (c) Results of 3D COMSOL simulations of the Cherenkov THz power intensity when outcoupled from the device into (b) Si and (c) air. Upper figures of (b) and (c) display the simulated magnetic field (H_x) of the THz output of the device, respectively.

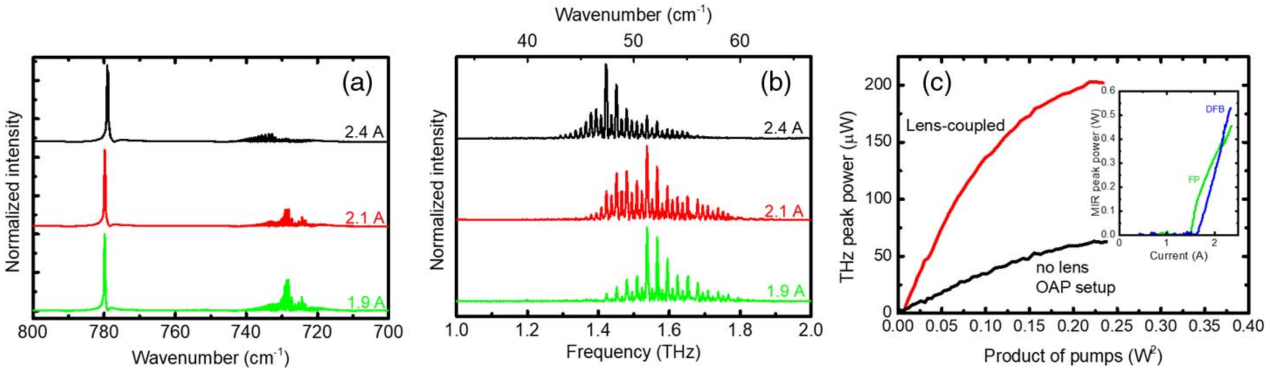

Fig. 3. Performance of a 3 mm long, 16 μm wide nonlinear-QCL with multimode spectra when operated at 288 K. Emission spectra for (a) MIR and (b) THz at various currents. (c) Peak THz output powers versus products of the MIR pump powers for the device with and without the Si lens.

using a screw clamp. The lens position was aligned roughly by monitoring the MIR output powers from the device using an infrared camera. Figures 2(b) and 2(c) show the results of a 3D COMSOL simulation of the Cherenkov THz emissions that are outcoupled into Si [shown in Fig. 2(b)] and the air [shown in Fig. 2(c)] from the polished facet of the device with a length of 500 μm when operating at 1.5 THz. The laser ridge width was assumed to be 16 μm and the waveguide structure used in the simulations was almost identical to the waveguide structure of the QCL device that was tested experimentally, although it was slightly simplified. The nonlinear THz polarization waves are simulated using DFG, where two MIR pumps propagate in the active region. The simulated THz output power for the extraction to Si was approximately three times as high as that for the extraction to air. These results indicate that the Si lens-coupled Cherenkov scheme enables much more efficient extraction than previous schemes.

Measurements of the device were taken using 250 ns current pulses at a repetition rate of 100 kHz to gather both MIR and THz data. The emission spectra of the device were measured using a Fourier transform IR (FTIR) spectrometer and recorded using a helium-cooled bolometer and a mercury cadmium telluride (MCT) infrared detector for the THz and MIR data, respectively. Figures 3(a) and 3(b) display the room-temperature MIR and THz spectra measured for the as-cleaved nonlinear QCL devices. Dual wavelength operation with peak wavelengths of ~730 and 780 cm^{-1} is observed for the device. We confirm that the peak wavelengths of the MIR pumps are identical for the devices with and without the Si lens. The THz emission from the device shows good agreement with the frequency separation of the MIR pumps. Figure 3(c) shows the THz power output as a function of the product of the two MIR pumps. The lens-coupled device produces 203 μW of peak output power with a 0.9 mW/W^2 MIR-to-THz conversion efficiency, which is defined as the ratio of the measured THz output power to the product of the two MIR pump powers, around the rollover point. The THz power of the lens-coupled device was measured with the bolometer positioned approximately 5 mm away from the Si lens. After removal of the Si lens, the device provides 62 μW peak output power with a conversion efficiency of 0.25 mW/W^2 when two off-axis parabolic (OAP) mirrors with 5 cm focal lengths were used to collect and refocus the THz output onto the bolometer in a nitrogen-purged environment (a maximum collection efficiency of ~70% is estimated). For the lens-coupled device, nearly 30% of the THz light is reflected at the Si/air interface. However, the THz output powers for both of these measurements are not corrected for the THz power measurements. Comparison of these results indicates improvement by a factor of ~3.3 in the THz power and conversion efficiency. A clear improvement has thus been observed for the lens-coupled device and this shows reasonable agreement with the simulation results, as shown in Figs. 2(c) and 2(d). The slightly higher THz power when compared with the value from the COMSOL simulations in Fig. 2 may be a result of the different collection efficiency for the THz measurement setup.

Figure 4 shows the measured far-field profiles of the no-lens and Si lens-coupled devices. These profiles were obtained by scanning a Golay cell at a distance of 5 cm from the laser facet. The device without the Si lens produced a far-field profile that was close to a Gaussian shape and the FWHM values for the device are 26° for the fast axis and 20° for the slow axis. In contrast to the results for Cherenkov QCL devices emitting at higher frequencies (>2.5 THz) [26,27,29], a narrower FWHM is observed along the slow axis; this may be because of the higher MIR group index ($n_g \sim 3.46$) of the device when compared to that of the QCL in the $\lambda \sim 10$ μm range ($n_g \sim 3.36$). The group index of the device is better matched to the THz refractive index value of the SI InP substrate. In contrast, the lens-coupled device shows beam widths that are approximately 2.5 times narrower than the case without the Si lens. The FWHM values of the lens-coupled device are 9.8° for the fast axis and 9.0° for the slow axis. Figure 5(a) depicts the temperature dependence of THz $I - V - L$ characteristics for the lens-coupled device in the 210–300 K temperature range when operating in the same pulsed mode (100 kHz, 250 ns). Figure 5(b) shows the THz spectra of the presented device when measured at different temperatures in the 210–288 K range, which can be obtained using a thermoelectric cooler (TEC). The results show a THz output power of approximately 0.5 mW at 210 K at emission frequencies in the 1.4–1.8 THz range. We observe that the maximum THz average power of >25 μW at 240 K is obtained at a duty cycle of 8%. The higher THz output power at lower

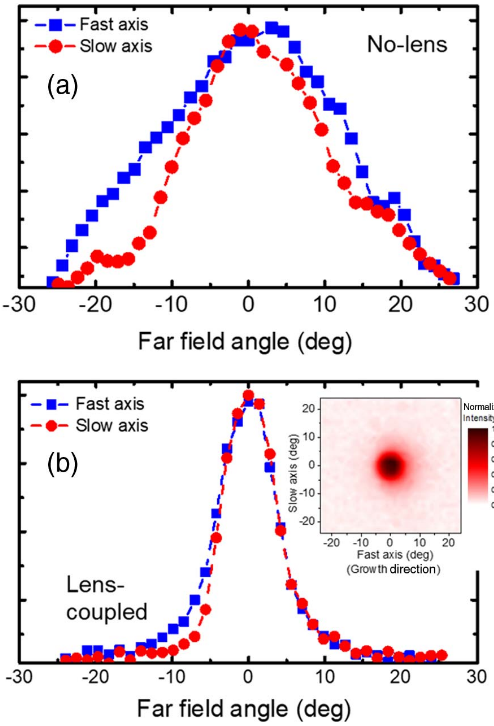

Fig. 4. Measured far-field beam patterns: (a) no-lens device and (b) lens-coupled device. A 2D far-field profile for the lens-coupled device is also shown in the inset.

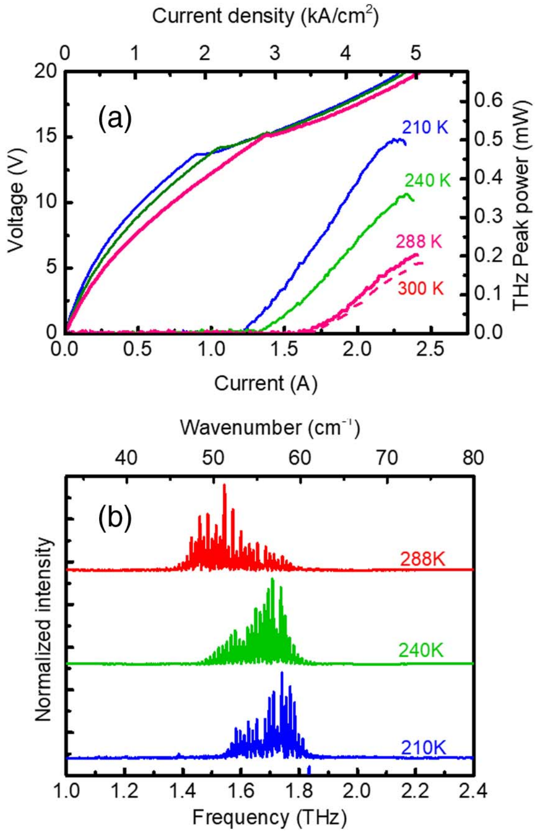

Fig. 5. (a) THz light output-current-voltage characteristics of the 16 μm wide and 3 mm long QCL device at different heat-sink temperatures when measured in pulsed mode (pulse width of 250 ns and repetition rate of 100 kHz). (b) THz spectra at different temperatures.

temperatures is attributed to the increased output pump powers for the MIR light, as shown in Fig. 1(a).

4. BROADLY TUNABLE SOURCE IN SUB-THz TO THz RANGE

The broadly tunable THz-QCL source based on DFG can be operated using an EC QCL system, which has been demonstrated for the frequency range from 1 to 6 THz [29,31]. Using a long-wavelength DAU QCL gain medium (3 mm long, 16 mm wide), which was taken from the same wafer described above, we constructed an EC setup using a Littrow configuration, similar to that of our previous work in MIR-QCLs [47]. A schematic of this setup is shown in Fig. 6(a). In the system, one MIR pump frequency (ω_{DFB}) is fixed using a monolithic DFB grating that was fabricated in the laser cavity, while the other MIR pump frequency (ω_{EC}) is tuned using an EC diffraction grating, where the THz radiation is achieved at a difference frequency of $\omega_{\mathrm{THz}} = \omega_{\mathrm{DFB}} - \omega_{\mathrm{EC}}$. The lens-coupled approach can be applied to the EC-QCL system. The collimating ZnSe aspheric lens that introduced the laser light to the external grating (100 grooves/mm) was anti-reflection (AR) coated and had a focal length of 1.8 mm. The grating period was designed to be constant to provide feedback at the MIR wavelength of 777 cm^{-1}. The EC was then used to vary the second lasing wavelength of the MIR pump (from 710 to 763 cm^{-1}). To suppress FP lasing, one of the cleaved facets was coated with an AR dielectric multilayer and the other facet was used as cleaved, and the substrate was polished to apply the Si lens-coupled scheme for THz extraction. Note here that the EC lens-coupled device configuration can technically be assembled within a butterfly-style package (dimensions: 13 mm × 30 mm × 13 mm) through application of a microelectromechanical systems (MEMS) external grating and associated optical mounting technology developed by our group [48].

Figure 6(b) shows the $I-L$ characteristics for the THz emission and the MIR pumps for the case when the EC grating is positioned to select the pump frequency at approximately 763 cm^{-1}, which corresponds to the lowest difference-frequency of the present work at approximately 14.1 cm^{-1} or 420 GHz, and is close to device gain peak. The MIR power increases as a function of the input current up to the rollover point and, as a result, a peak THz power of approximately 15 μW is obtained. The inset in Fig. 6(b) shows the THz emission spectrum recorded at 2.4 A and 293 K. The operating frequency of 420 GHz at room temperature is the lowest reported in monolithic THz DFG sources based on MIR QCLs. The MIR spectra and powers of the mid-infrared pumps at ω_{EC} and ω_{DFB} are shown in Fig. 6(c) for various grating angles. The spectra were measured at room temperature at a pump current of 2.4 A, which is close to the rollover point. The corresponding THz spectra in Fig. 6(d) show the recorded emission spectra of the EC QCL system for operation between 0.42 and 2.0 THz. Single-frequency emission with a side-mode suppression ratio of more than 10 dB is observed for nearly all the THz

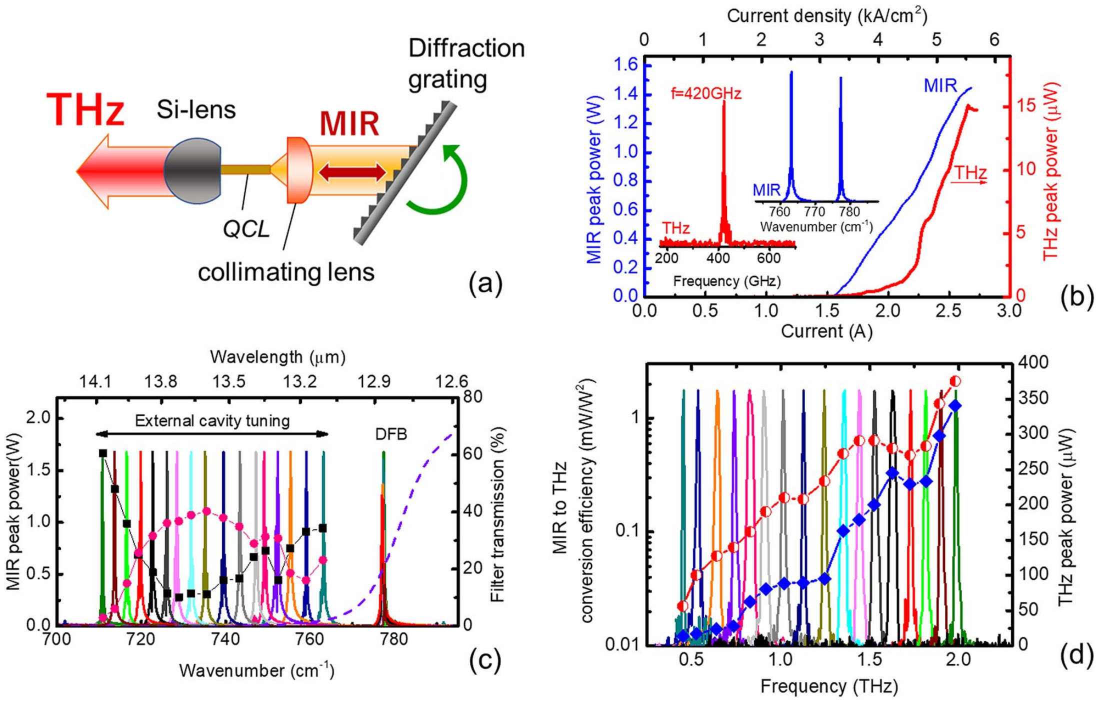

Fig. 6. (a) Schematic of Si lens-coupled EC system setup used in the experiments. (b) Light output-current characteristics of the MIR and THz emissions from the THz EC system with a nonlinear QCL when operating at 420 GHz. The THz emission spectrum measured at a current density of 5.0 kA/cm^2 is also shown in the inset. (c) MIR emission spectra and power outputs from the two MIR pumps for the EC nonlinear-QCL system described in (a) at different EC diffraction grating positions. The MIR powers for ω_{DFB} (black squares) and ω_{EC} (red circles) pumps are shown as a function of the ω_{EC} pump wavenumber. The dashed line represents the transmission spectrum of the MIR short-pass filter. (d) THz emission spectra of the EC nonlinear-QCL system at a current density of 5.0 kA/cm^2. The THz peak power (blue diamonds and right axis) and the MIR-to-THz conversion efficiency (red-white circles and left axis) are also plotted as a function of the THz frequency.

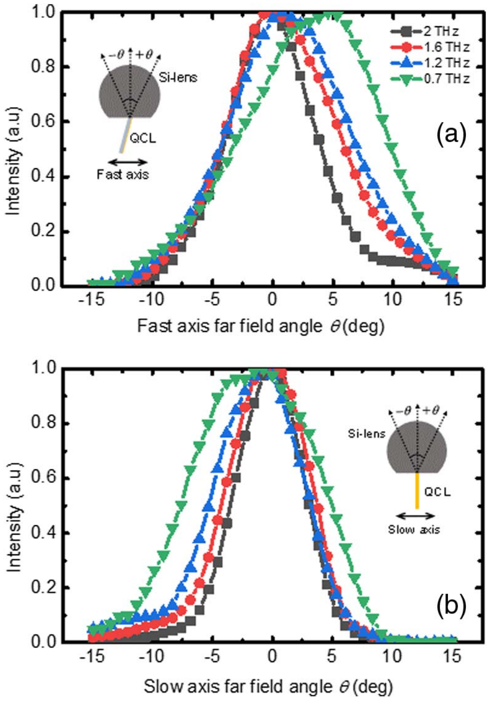

Fig. 7. Far-field THz emission profile of the EC lens-coupled QCL device described in Fig. 6: (a) vertical and (b) horizontal. The vertical angle θ is defined relative to the direction normal to the laser facet, as shown in the right inset of (a).

signals. The measured power at each THz wavelength varies from 15 µW at 420 GHz to 0.25 mW at 2 THz. The MIR to THz conversion efficiency is maximized at the highest frequency peaks at 2 THz with a value of 2.0 mW/W^2, and decreases toward the lower frequencies; this is a result of the decreasing nonlinearity and the increasing optical absorption occurring in the doped QCL waveguide [39].

The far-field THz emission profile of the EC tuned lens-coupled device is shown in Fig. 7 for the vertical [Fig. 7(a)] and horizontal [Fig. 7(b)] directions. Significant broadening of the FWHM of the beam profiles in both the vertical and horizontal directions is observed when the THz emission frequency is reduced. The far-field angle in the vertical direction is steered with the THz emission frequency by varying the angle of the Cherenkov DFG emission into the InP substrate [31]. Although it is difficult to estimate the steering angle for the lens-coupled device, the peak of the beam patterns is steered according to the angle of the Cherenkov DFG emission.

5. CONCLUSION

In conclusion, we have reported widely tunable THz nonlinear QCLs using a Si lens-coupled Cherenkov waveguide scheme. As a result of the significant enhancement of the THz coupling efficiency, the lens-coupled device exhibits a THz output power that is ~3.3 times higher and improved conversion efficiency when compared to the corresponding quantities of the device without the Si lens. Relying on a high-power, long-wavelength

QCL, a room-temperature device emitting at 1.5 THz provided 0.2 mW peak output power with a high-quality beam pattern. Additionally, we constructed an EC setup that incorporated the Si lens-coupled gain medium for frequency tuning in the low-frequency region below 2 THz. As a result, we achieved wide frequency tuning of between 0.42 and 2 THz. The operating frequency of 420 GHz is the lowest reported operating frequency for room-temperature QCL sources. In the near future, a much wider tuning range toward the higher frequency direction could be made possible by optimizing the gain medium and the position of the DFB emission. Furthermore, different lens coupling configurations could be adopted for more efficient outcoupling, including metasurface technology [49]. By improving all these aspects of the devices, this technology can bridge the THz gap and may open up new application areas for THz technology.

Funding. Strategic Information and Communications R&D Promotion Programme (SCOPE) (JP195006001).

Acknowledgment. The authors acknowledge Dr. T. Edamura, Dr. H. Fujiwara, and Dr. H. Satozono for their helpful comments. The authors also wish to acknowledge Dr. K. Kuroyanagi for assistance with running the silicon bolometer setup. The authors thank A. Sugiyama for carrying out the AR coating and for fabrication of the EC grating, and David MacDonald, MSc, from Edanz for editing a draft of this paper.

Disclosures. The authors declare no conflicts of interest.

Data Availability. Data underlying the results presented in this paper are not publicly available at this time but may be obtained from the authors upon reasonable request.

REFERENCES

1. M. Tonouchi, "Cutting-edge terahertz technology," Nat. Photonics **1**, 97–105 (2007).
2. S. Dhillon, M. Vitiello, E. Linfield, A. Davies, M. C. Hoffmann, J. Booske, C. Paoloni, M. Gensch, P. Weightman, and G. Williams, "The 2017 terahertz science and technology roadmap," J. Phys. D **50**, 043001 (2017).
3. T. Maekawa, H. Kanaya, S. Suzuki, and M. Asada, "Oscillation up to 1.92 THz in resonant tunneling diode by reduced conduction loss," Appl. Phys. Express **9**, 024101 (2016).
4. K. Kasagi, S. Suzuki, and M. Asada, "Large-scale array of resonant-tunneling-diode terahertz oscillators for high output power at 1 THz," J. Appl. Phys. **125**, 151601 (2019).
5. P. Chevalier, M. Schröter, C. R. Bolognesi, V. d'Alessandro, M. Alexandrova, J. Böck, R. Flückiger, S. Fregonese, B. Heinemann, and C. Jungemann, "Si/SiGe:C and InP/GaAsSb heterojunction bipolar transistors for THz applications," Proc. IEEE **105**, 1035–1050 (2017).
6. M. Urteaga, Z. Griffith, M. Seo, J. Hacker, and M. J. Rodwell, "InP HBT technologies for THz integrated circuits," Proc. IEEE **105**, 1051–1067 (2017).
7. Z. Hu, M. Kaynak, and R. Han, "High-power radiation at 1 THz in silicon: a fully scalable array using a multi-functional radiating mesh structure," IEEE J. Solid-State Circuits **53**, 1313–1327 (2018).
8. R. Han and E. Afshari, "A CMOS high-power broadband 260-GHz radiator array for spectroscopy," IEEE J. Solid-State Circuits **48**, 3090–3104 (2013).
9. U. R. Pfeiffer, Y. Zhao, J. Grzyb, R. Al Hadi, N. Sarmah, W. Förster, H. Rücker, and B. Heinemann, "A 0.53 THz reconfigurable source module with up to 1 mW radiated power for diffuse illumination in terahertz imaging applications," IEEE J. Solid-State Circuits **49**, 2938–2950 (2014).
10. K. Sengupta, T. Nagatsuma, and D. M. Mittleman, "Terahertz integrated electronic and hybrid electronic–photonic systems," Nat. Electron. **1**, 622–635 (2018).
11. S. Hayashi, K. Nawata, Y. Takida, Y. Tokizane, K. Kawase, and H. Minamide, "High-brightness continuously tunable narrowband subterahertz wave generation," IEEE Trans. Terahertz Sci. Technol. **6**, 858–861 (2016).
12. M. Scheller, J. M. Yarborough, J. V. Moloney, M. Fallahi, M. Koch, and S. W. Koch, "Room temperature continuous wave milliwatt terahertz source," Opt. Express **18**, 27112–27117 (2010).
13. A. Maestrini, I. Mehdi, J. V. Siles, R. Lin, C. Lee, G. Chattopadhyay, J. Pearson, and P. Siegel, "Frequency tunable electronic sources working at room temperature in the 1 to 3 THz band," Proc. SPIE **8496**, 84960F (2012).
14. L. Bosco, M. Franckié, G. Scalari, M. Beck, A. Wacker, and J. Faist, "Thermoelectrically cooled THz quantum cascade laser operating up to 210 K," Appl. Phys. Lett. **115**, 010601 (2019).
15. A. Khalatpour, A. K. Paulsen, C. Deimert, Z. R. Wasilewski, and Q. Hu, "High-power portable terahertz laser systems," Nat. Photonics **15**, 16–20 (2020).
16. C. Walther, G. Scalari, J. Faist, H. Beere, and D. Ritchie, "Low frequency terahertz quantum cascade laser operating from 1.6 to 1.8 THz," Appl. Phys. Lett. **89**, 231121 (2006).
17. A. Pagies, G. Ducournau, and J.-F. Lampin, "Low-threshold terahertz molecular laser optically pumped by a quantum cascade laser," APL Photon. **1**, 031302 (2016).
18. P. Chevalier, A. Amirzhan, F. Wang, M. Piccardo, S. G. Johnson, F. Capasso, and H. O. Everitt, "Widely tunable compact terahertz gas lasers," Science **366**, 856–860 (2019).
19. J.-F. Lampin, A. Pagies, G. Santarelli, J. Hesler, W. Hansel, R. Holzwarth, and S. Barbieri, "Quantum cascade laser-pumped terahertz molecular lasers: frequency noise and phase-locking using a 1560 nm frequency comb," Opt. Express **28**, 2091–2106 (2020).
20. H. Ito, T. Yoshimatsu, H. Yamamoto, and T. Ishibashi, "Widely frequency tunable terahertz-wave emitter integrating uni-traveling-carrier photodiode and extended bowtie antenna," Appl. Phys. Express **6**, 064101 (2013).
21. T. Nagatsuma, G. Ducournau, and C. C. Renaud, "Advances in terahertz communications accelerated by photonics," Nat. Photonics **10**, 371–379 (2016).
22. M. A. Belkin, F. Capasso, A. Belyanin, D. L. Sivco, A. Y. Cho, D. C. Oakley, C. J. Vineis, and G. W. Turner, "Terahertz quantum-cascade-laser source based on intracavity difference-frequency generation," Nat. Photonics **1**, 288–292 (2007).
23. M. A. Belkin, F. Capasso, F. Xie, A. Belyanin, M. Fischer, A. Wittmann, and J. Faist, "Room temperature terahertz quantum cascade laser source based on intracavity difference-frequency generation," Appl. Phys. Lett. **92**, 201101 (2008).
24. Q. Y. Lu, N. Bandyopadhyay, S. Slivken, Y. Bai, and M. Razeghi, "Room temperature single-mode terahertz sources based on intracavity difference-frequency generation in quantum cascade lasers," Appl. Phys. Lett. **99**, 131106 (2011).
25. M. A. Belkin and F. Capasso, "New frontiers in quantum cascade lasers: high performance room temperature terahertz sources," Phys. Scr. **90**, 118002 (2015).
26. Q. Lu and M. Razeghi, "Recent advances in room temperature, high-power terahertz quantum cascade laser sources based on difference-frequency generation," Photonics **3**, 42 (2016).
27. K. Fujita, S. Jung, Y. Jiang, J. H. Kim, A. Nakanishi, A. Ito, M. Hitaka, T. Edamura, and M. A. Belkin, "Recent progress in terahertz difference-frequency quantum cascade laser sources," Nanophotonics **7**, 1795–1817 (2018).
28. K. Vijayraghavan, R. W. Adams, A. Vizbaras, M. Jang, C. Grasse, G. Boehm, M. C. Amann, and M. A. Belkin, "Terahertz sources based on Čerenkov difference-frequency generation in quantum cascade lasers," Appl. Phys. Lett. **100**, 251104 (2012).

29. K. Vijayraghavan, Y. Jiang, M. Jang, A. Jiang, K. Choutagunta, A. Vizbaras, F. Demmerle, G. Boehm, M. C. Amann, and M. A. Belkin, "Broadly tunable terahertz generation in mid-infrared quantum cascade lasers," Nat. Commun. **4**, 2021 (2013).
30. K. Fujita, M. Hitaka, A. Ito, T. Edamura, M. Yamanishi, S. Jung, and M. A. Belkin, "Terahertz generation in mid-infrared quantum cascade lasers with a dual-upper-state active region," Appl. Phys. Lett. **106**, 251104 (2015).
31. Y. Jiang, K. Vijayraghavan, S. Jung, F. Demmerle, G. Boehm, M. C. Amann, and M. A. Belkin, "External cavity terahertz quantum cascade laser sources based on intra-cavity frequency mixing with 1.2–5.9 THz tuning range," J. Opt. **16**, 094002 (2014).
32. Q. Y. Lu, N. Bandyopadhyay, S. Slivken, Y. Bai, and M. Razeghi, "Widely tuned room temperature terahertz quantum cascade laser sources based on difference-frequency generation," Appl. Phys. Lett. **101**, 251121 (2012).
33. Q. Lu, D. Wu, S. Sengupta, S. Slivken, and M. Razeghi, "Room temperature continuous wave, monolithic tunable THz sources based on highly efficient mid-infrared quantum cascade lasers," Sci. Rep. **6**, 23595 (2016).
34. K. Fujita, M. Hitaka, A. Ito, M. Yamanishi, T. Dougakiuchi, and T. Edamura, "Ultra-broadband room-temperature terahertz quantum cascade laser sources based on difference frequency generation," Opt. Express **24**, 16357–16365 (2016).
35. L. Consolino, M. Nafa, M. De Regis, F. Cappelli, S. Bartalini, A. Ito, M. Hitaka, T. Dougakiuchi, T. Edamura, P. De Natale, and K. Fujita, "Direct observation of terahertz frequency comb generation in difference-frequency quantum cascade lasers," Appl. Sci. **11**, 1416 (2021).
36. Q. Lu, F. Wang, D. Wu, S. Slivken, and M. Razeghi, "Room temperature terahertz semiconductor frequency comb," Nat. Commun. **10**, 2403 (2019).
37. A. Nakanishi, K. Fujita, K. Horita, and H. Takahashi, "Terahertz imaging with room-temperature terahertz difference-frequency quantum-cascade laser sources," Opt. Express **27**, 1884–1893 (2019).
38. A. Nakanishi, S. Hayashi, H. Satozono, and K. Fujita, "Spectroscopic imaging with an ultra-broadband (1–4 THz) compact terahertz difference-frequency generation source," Electronics **10**, 336 (2021).
39. K. Fujita, S. Hayashi, A. Ito, M. Hitaka, and T. Dougakiuchi, "Sub-terahertz and terahertz generation in long-wavelength quantum cascade lasers," Nanophotonics **8**, 2235–2241 (2019).
40. S. Hayashi, A. Ito, M. Hitaka, and K. Fujita, "Room temperature, single-mode 1.0 THz semiconductor source based on long-wavelength infrared quantum-cascade laser," Appl. Phys. Express **13**, 112001 (2020).
41. V. Pistore, H. Nong, P.-B. Vigneron, K. Garrasi, S. Houver, L. Li, A. G. Davies, E. H. Linfield, J. Tignon, and J. Mangeney, "Millimeter wave photonics with terahertz semiconductor lasers," Nat. Commun. **12**, 1427 (2021).
42. K. Fujita, T. Edamura, S. Furuta, and M. Yamanishi, "High-performance, homogeneous broad-gain quantum cascade lasers based on dual-upper-state design," Appl. Phys. Lett. **96**, 241107 (2010).
43. S. Niu, J. Liu, F. Cheng, H. Wang, J. Zhang, N. Zhuo, S. Zhai, L. Wang, S. Liu, and F. Liu, "14 μm quantum cascade lasers based on diagonal transition and nonresonant extraction," Photon. Res. **7**, 1244–1248 (2019).
44. A. W. M. Lee, Q. Qin, S. Kumar, B. S. Williams, Q. Hu, and J. L. Reno, "High-power and high-temperature THz quantum-cascade lasers based on lens-coupled metal-metal waveguides," Opt. Lett. **32**, 2840–2842 (2007).
45. D. B. Rutledge, D. P. Neikirk, and D. P. Kasilingam, "Integrated circuit antennas," in *Infrared and Millimeter Waves* (Academic, 1983), Vol. **10**, pp. 1–90.
46. S. Jung, J. H. Kim, Y. Jiang, K. Vijayraghavan, and M. A. Belkin, "Terahertz difference-frequency quantum cascade laser sources on silicon," Optica **4**, 38–43 (2016).
47. T. Dougakiuchi, K. Fujita, A. Sugiyama, A. Ito, N. Akikusa, and T. Edamura, "Broadband tuning of continuous wave quantum cascade lasers in long wavelength (> 10 μm) range," Opt. Express **22**, 19930–19935 (2014).
48. Hamamatsu Photonics K.K., "The world's smallest wavelength-swept quantum cascade laser (QCL) mountable in small spaces as a light source designed for portable volcanic gas monitoring systems," https://www.hamamatsu.com/jp/en/news/products-and-technologies/2021/20210817000000.html (2021).
49. K. Endo, M. Sekiya, J. Kim, K. Sato, and T. Suzuki, "Resonant tunneling diode integrated with metalens for high-directivity terahertz waves," Appl. Phys. Express **14**, 082001 (2021).